

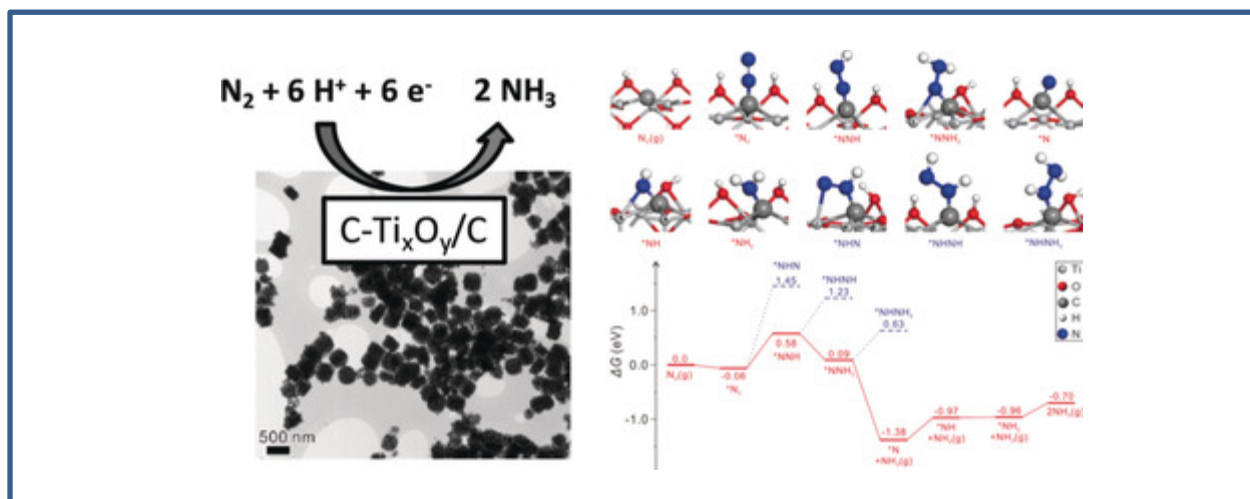


Published in final edited form as:

Qin, Q., Zhao, Y., Schmallegger, M., Heil, T., Schmidt, J., Walczak, R., et al. (2019). Enhanced electrocatalytic N₂ reduction via partial anion substitution in titanium oxide-carbon composites. *Angewandte Chemie International Edition*, 58(37), 13101-13106. doi:10.1002/anie.201906056.

Enhanced electrocatalytic N₂ reduction via partial anion substitution in titanium oxide-carbon composites

Qing Qin, Yun Zhao, Max Schmallegger, Tobias Heil, Johannes Schmidt, Ralf Walczak, Georg Gescheidt-Demner, Haijun Jiao, Martin Oschatz



Partial anion substitution in titanium oxide-carbon composites is reported as a novel mode to activate dinitrogen and enhance its electrocatalytic reduction to ammonia.

Enhanced electrocatalytic N₂ reduction via partial anion substitution in titanium oxide-carbon composites

Qing Qin,^{1†} Yun Zhao,^{2†} Max Schmallegger,³ Tobias Heil,¹ Johannes Schmidt,⁴ Ralf Walczak,¹ Georg Gescheidt-Demner,³ Haijun Jiao,² and Martin Oschatz^{1,5*}

Abstract: The electrochemical conversion of N₂ at ambient conditions using renewably generated electricity is an attractive approach for sustainable ammonia (NH₃) production. Considering the chemical inertness of N₂, rational design of efficient catalysts is required. Therefore, in this work, it is demonstrated that a C-doped TiO₂/C (C-Ti_xO_y/C) material derived from MIL-125(Ti) metal-organic framework (MOF) can achieve a high Faradaic efficiency (FE) of 17.8 %, which even surpasses most of the established noble metal-based catalysts. On the basis of the experimental results and theoretical calculations, the remarkable properties of the catalysts can be attributed to the doping of carbon atoms into oxygen vacancies (OVs) and the formation of Ti-C bonds in C-Ti_xO_y. This binding motive is found to be energetically more favorable for N₂ activation compared to the non-substituted OVs in TiO₂. This work elucidates that electrochemical N₂ reduction reaction (NRR) performance can be largely improved by creating catalytically active centers through rational substitution of anions into metal oxides.

As expressed by its annual worldwide production exceeding 145 million tons, NH₃ plays an extremely important role in agricultural fertilizers, fuels, as hydrogen carrier and in many other fields.^[1] The industrially applied Haber-Bosch process suffers from the need for high temperature and pressure. Furthermore, whereas the Haber-Bosch process itself produces a lot of energies which can be recovered, the production of molecular hydrogen by reforming causes large energy consumption and carbon dioxide emissions. Hence, NRR in which nitrogen is reduced with protons and electrons instead of molecular hydrogen at ambient conditions by using renewable electricity is emerging as an alternative technology towards a more sustainable NH₃ production.^[2] However, the difficulty to polarize the N₂ molecule makes it difficult to be activated and this is the main reason for the so far limited efficiency and space-time yield of NRR.^[3] In aqueous solution, the increase of the electric potential to enhance the activation of N₂ is an option of limited applicability as

NRR under these conditions is largely inhibited by the competitive hydrogen evolution reaction (HER).^[4] Because of this, developing efficient NRR catalysts has attracted increasing attention. The ultimate requirement to such types of catalysts is to bind and polarize N₂ molecules in a way that the electron density within the molecule is shifted facilitating the reaction with protons and/or electrons.^[5] Until now, various promising catalysts have been investigated for electrochemical NRR, including metals,^[6] metal oxides,^[7] metal nitrides,^[8] metal carbides,^[9] metal complexes^[10] and carbon-based materials.^[11] Among them, noble metals exhibit favorable NRR performance,^[6] but considering the cost, they are not suitable for large-scale implementation of NRR. Alternative strategies can be either to construct single atom catalytic sites to decrease the amount of noble metal used or develop non-noble metal based materials.^[11a, 12] The latter has attracted more interests recently.^[6, 13] Although some non-noble metal based materials have proven to be efficient catalysts for electrochemical NRR,^[9b] more detailed mechanistic understanding is still needed for guiding the design of new-generation NRR electrocatalysts.

As the second most abundant transition metal in the earth's crust, Ti-based materials can be potential candidates due to their stronger binding towards N-adatoms than H-adatoms leading to better N₂ reducing ability.^[2c] Thus, MXenes with a great number of exposed edge sites have been used as efficient NRR electrocatalyst.^[9b] In addition, TiO₂ has also been studied for their application in electrochemical NRR and oxygen vacancies (OVs) are demonstrated to be pivotal to N₂ activation.^[14] However, achieving a higher FE of these Ti-based materials is still a big challenge, which means that the construction of more effective Ti-based active sites is highly required. Our inspiration for a novel synthesis scheme for Ti-based NRR catalysts is coming from the versatile redox chemistry of oxygen-deficient titanium oxides. The wide distribution of possible electronic band structures as well as many possible anionic substitutions will provide abundant active sites for N₂ activation.^[15] Furthermore, previous reports have shown that MOF-derived catalysts have tunable porosity, high surface area, controllable functionalization, as well as good conductivity and thus provide great potential as electrocatalysts.^[16] To the best of our knowledge, Ti-MOF-derived materials have not been used in electrochemical NRR yet.

Ti₈O₈(OH)₄(BDC)₆ (MIL-125(Ti)) (BDC = benzene-1,4-dicarboxylate) (Scheme S1) has been chosen as the MOF precursor and a novel NRR electrocatalyst based on a carbon-doped, oxygen deficient titanium oxide/carbon (C-Ti_xO_y/C) nanohybrid was prepared via a one-step thermal conversion with rich (O-)Ti-C bonds and OVs. Such partial anion substitution leads to excellent electrochemical NRR performance with highest FE of 17.8 % and a remarkable NH₃ production rate of 14.8 μg h⁻¹ mg⁻¹ cat. The crucial role of carbon substitution in electrochemical NRR is proven for the first time by a combination of experimental and density functional theory (DFT) results.

- [1] Q. Qin, Dr. T. Heil, R. Walczak, Dr. M. Oschatz
Max Planck Institute of Colloids and Interfaces, Department of Colloid Chemistry, Am Mühlenberg 1, 14476, Potsdam, Germany
E-Mail: martin.oschatz@mpikg.mpg.de
- [2] Dr. Y. Zhao, Dr. H. Jiao
Leibniz-Institut für Katalyse e.V. an der Universität Rostock, Albert-Einstein-Straße 29a, Rostock, 18059, Germany
- [3] M. Schmallegger, Prof. G. Gescheidt
Graz University of Technology, Institute of Physical and Theoretical Chemistry, NAWI Graz, Stremayrgasse 9, 8010, Graz, Austria
- [4] Dr. J. Schmidt
Technische Universität Berlin, Institute of Chemistry, Division of Functional Materials, Hardenbergstraße 40, 10623, Berlin, Germany
- [5] Dr. M. Oschatz
Universität Potsdam, Institute of Chemistry, Karl-Liebknecht-Straße 24-25, 14476 Potsdam, Germany
- †Q. Qin and Y. Zhao contribute equally to this work.
Supporting information for this article is given via a link at the end of

MIL-125(Ti) was synthesized according to the literature (see Supporting Information for more details) (Figure S1).^[17] C-Ti_xO_y/C hybrid nanostructures (denoted as M-Ts with T representing the pyrolysis temperature) were synthesized by annealing MIL-125(Ti) at 800, 900, 1000 and 1100 °C for 2 h under Ar atmosphere. Transmission electron microscopy (TEM) (Figure 1a-b) and scanning electron microscopy (SEM) images (Figure S2) of as-obtained M-1000 reveal that the transformed MOF particles become much looser but retain the polyhedral geometry of the former MIL-125(Ti) crystals with an average size of 300 nm and contain some smaller nanoparticles. High-resolution TEM (HRTEM) images show that TiO₂ nanoparticles with sizes between 3 and 20 nm are well-dispersed in an amorphous environment with exposed (110) facets (Figure 1c). TEM images of M-800, M-900 and M-1100 also exhibit a comparable structure (Figure S3).

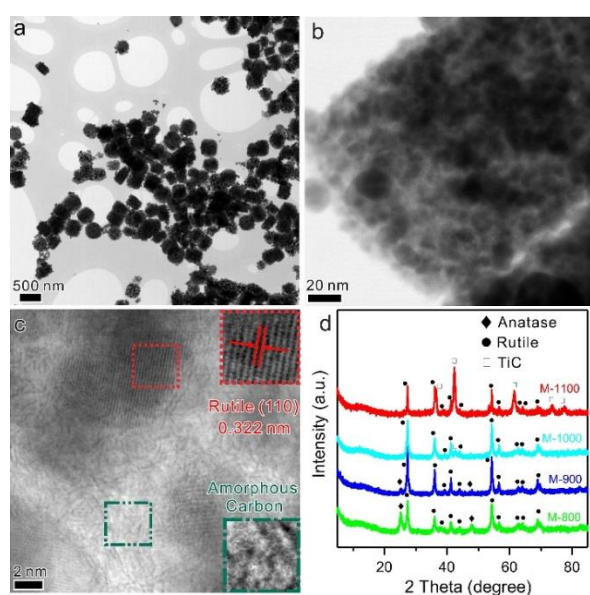


Figure 1. (a-c) Representative TEM images of M-1000. The insets of c are the corresponding HRTEM images of the marked square areas. (d) XRD patterns of M-Ts.

The X-ray diffraction (XRD) patterns of as-obtained samples (Figure 1d) indicate that M-800 are TiO₂-containing nanocomposites consisting of tetragonal Rutile (JCPDS No. 21-1276) and tetragonal Anatase (JCPDS No. 21-1272).^[18] For M-900, the diffraction peaks of Anatase become much weaker, while only diffraction peaks of Rutile appear in M-1000 and M-1100. Notably, because of the carbothermal reduction of TiO₂, a small new diffraction peak at 43.5° appears in M-1000, which can be attributed to TiC.^[19] With further increasing temperature, M-1100 shows more intense diffraction peaks of TiC, as its content increases at higher temperature due to the faster carbothermal reduction. Raman spectra of the as-obtained materials (Figure 2a) all exhibit three main bands centered at approximately 249, 413, and 601 cm⁻¹. By comparison of the Raman spectra of TiC, Anatase, and Rutile with M-1000 (Figure S4), it can also be concluded that Ti-C and Ti-O bonds may coexist in M-Ts due to the small Raman shift.^[20] Besides, two small bands at ~1350 and 1590 cm⁻¹ are assigned to disordered

(D) and graphite (G)-like bands of free carbon.^[21] It is worth to note that the latter bands almost disappear in M-1100, as more free carbon reacts with TiO₂ to form TiC at higher temperature. The formation process of M-Ts can also be followed by thermogravimetric analysis (TGA) (Figure S5). Besides, TGA under air was carried out to investigate the structures of M-Ts (Figure 2b). Notably, there is an obvious increase in mass within the temperature range between 164 and 316 °C for M-1000 and M-1100. This can be ascribed to the oxidation and substitution of carbon doped into TiO₂ as well as the carbon in TiC.^[22] The higher increase in weight for M-1100 than for M-1000 indicates the higher carbide content in the former which is in line with the XRD results. In addition, the temperature of substitution of carbon shifts to higher values for M-1100 indicating the higher thermodynamic barrier for re-oxidation in TiC than in C-Ti_xO_y. N₂ (-196 °C) physisorption curves (Figure S6) display that M-Ts still have a porous structure with high SSA.

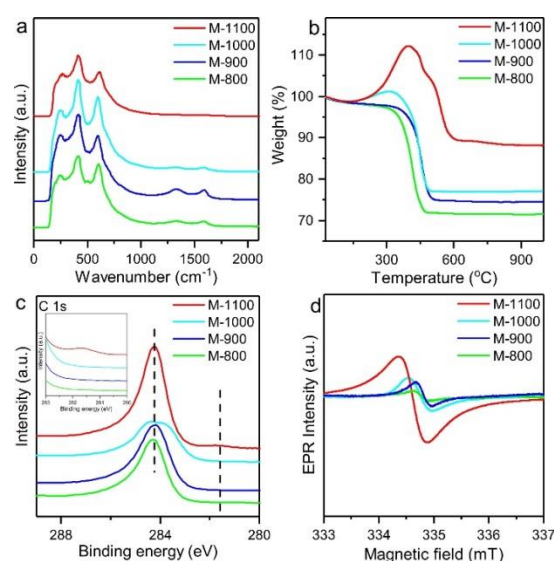
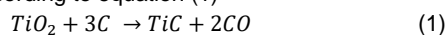


Figure 2. (a) Raman spectra, (b) TGA analysis (under synthetic air with a heating rate of 10 °C min⁻¹), (c) XPS spectra of C 1s and (d) EPR spectra for M-800, M-900, M-1000 and M-1100.

X-ray photoelectron spectroscopy (XPS) measurements were further performed to investigate the binding states of the elements present in the hybrid materials (Figure S7). The significant peak broadening of C 1s in M-1000 could be attributed to the presence of negatively polarized carbon atoms substituting oxygen in the anionic lattice of Rutile (Figure 2c).^[23] This broadening is not observed anymore in M-1100 but instead a new peak centered at 281.7 eV appears due to the existence of carbidic carbon in TiC with rather covalent character.^[24] High-resolution C 1s spectra of M-800, M-900 and M-1000 are mainly composed of four characteristic peaks (Figure S8), corresponding to the C-C, C-O, C=O, and O-Ti-C structures, respectively.^[25] Besides the above four peaks, a new characteristic peak assigned to Ti-C appears in M-1100 (Figure S8).^[24] Similarly, XPS spectra of Ti 2p (Figure S9) also show a significant peak broadening for M-1000 due to an increasing portion of Ti atoms bonded to carbon instead of the more electronegative oxide anions. This indicates that the content of

such “weakly anionic” carbon species is the highest in M-1000. Besides, M-1100 shows a new peak centered at 455.2 eV, which can again be attributed to the presence of oxygen-free TiC.^[24] The same peak broadening effect along with a minor binding energy shift is also seen in the XPS spectra of O 1s (Figure S10). Furthermore, the structure and reactivity of paramagnetic species were characterized at atomic level by electron paramagnetic resonance (EPR), which shows similar signals for M-800, M-900, M-1000 and M-1100 (g factors of 2.0038, 2.0040, 2.0043 and 2.0050, respectively) in EPR spectra (Figure 2d). They are not resolved and essentially indicate an isotropic line shape, which is in line with Ti³⁺ centers being possibly present in C-Ti_xO_y.^[26] The EPR intensity increases from M-800 to M-1100 revealing that treatment at higher temperature can induce higher concentration of OVs in the M-Ts.

Based on the above analysis, the formation of the M-Ts nanocomposites could thus be understood as follows: Ti in MIL-125(Ti) reacts with the nearby oxygen and aggregates into stable TiO₂ nanoparticles. Meanwhile, the organic ligands also undergo pyrolysis under high temperature to obtain pristine porous carbon, which can substitute the oxygen in TiO₂ to form OVs, and formed OVs can be further occupied by other carbon atoms. At temperature above 1000 °C, not only partial anion substitution takes place but then TiO₂ can be completely converted to TiC according to equation (1)



Besides, as the amount of OVs increases with higher temperature, the amount of C-Ti_xO_y also increases from T-800 to M-1000. Although TiC starts forming at 1000 °C, the amount is quite low as XPS results show. When the temperature is increased to 1100 °C, the free carbon is fully consumed, thus transfer of carbon atoms to OVs is inhibited even though more OVs may form at such high temperature.

For comparison, the gas flow during pyrolysis was changed from Ar to N₂ and the corresponding samples with nearly similar pore structure (Figure S11a) are denoted as M-Ts-N₂. As shown in XRD patterns, the diffraction peaks of TiN appear in M-900-N₂ and M-1000-N₂ (Figure S11b). Furthermore, elemental analysis (Table S1) also indicates a significant content of N in as-obtained M-Ts-N₂, and the amount of N increases with the increase of temperature. As there is no N species existing in the MOF precursor and M-Ts synthesized under argon atmosphere, the N₂ gas obviously participates in the calcination reaction of MOF precursor.

Our idea to use this material for electrochemical NRR is motivated by this versatile chemistry of the anion-substituted titanium oxides and the possible high affinity of the M-Ts towards N₂. The catalytic performance in the electrochemical NRR was firstly tested for M-1000 by using a H-cell with three-electrode system. As shown in the linear sweep voltammetry (LSV) curves in Ar and N₂-saturated 0.1 M LiClO₄ aqueous solution, there is an obvious intense response in current densities under N₂ (Figure S12). Chronoamperometry tests (Figure S13) were also carried out to calculate NH₃ yields and corresponding FEs, based on NH₄⁺ calibration curves (Figure S14). The maximum FE of 17.8% with a remarkable production rate of 14.8 μg h⁻¹ mg⁻¹_{cat.} for NH₃ is achieved at -0.4 V vs. RHE (Figure 3a). Besides, no N₂H₄ is detected as potential product as there is no obvious colour change before and after electrolysis when adding N₂H₄ colour

reagent (Figure S15a). UV-Vis spectra also confirm that no N₂H₄ is produced independent of the applied potential (Figure S15b). At more negative potentials, FE and NH₃ production rate are both cast into shade due to the strong competition with HER, which is indicated by the largely increased FE and H₂ production rate of hydrogen evolution (Figure S16a).^[27] As shown in the UV-Vis spectra (Figure 3b) and optical images (Figure S17), NH₄⁺ cannot be detected under different control experiments. Meanwhile, there is no NH₃ produced in Ar-saturated electrolyte at all given potentials (Figure S18). In addition, a ¹⁵N isotopic labelling experiment has been performed to verify the nitrogen source of the produced NH₃ (Figure 3c). The ¹H nuclear magnetic resonance (¹H NMR) spectra of standard samples show a triplet coupling for ¹⁴NH₄⁺ and a double coupling for ¹⁵NH₄⁺. The use of ¹⁴N₂ and ¹⁵N₂ as the feeding gas yields ¹⁴NH₄⁺ and ¹⁵NH₄⁺, respectively. Based on these NMR results, it is verified that the detected NH₃ is exclusively produced from the reduction of the introduced N₂ and possible formation of NH₃ from the traces of nitrogen present in M-1000 can be ruled out. In addition, based on the rigorous protocol for NH₃ synthesis,^[28] a control experiment has been performed by using ¹⁵N₂ and ¹⁴N₂ feeding gases separately and carrying out the chronoamperometry tests under the same conditions. The results show nearly the same FE and NH₃ production rate according to the calibration curve of the ¹H NMR signal for ¹⁵NH₄⁺ standard solutions, which also excludes the possible presence of impurities from ¹⁵N₂ gas (Figure S19). In the recycling test (Figure S20), no obvious fluctuation arises in the FE and NH₃ production rate (Figure 3d), demonstrating the good stability of M-1000 during the NRR, which can be also confirmed by continuous production of NH₃ during the long-term chronoamperometry test (Figure S21). TEM images acquired after the test demonstrate the structural stability as well (Figure S22).

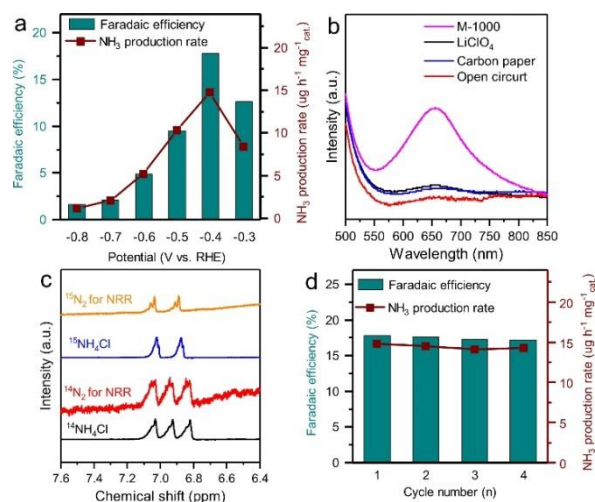


Figure 3. Electrochemical NRR performance of M-1000 electrode. (a) FE and NH₃ production rate at each given potential. (b) UV-Vis absorption spectra of the 0.1 M LiClO₄ solution with indophenol indicator after charging at -0.4 V vs. RHE for 10000 s under various conditions. (c) ¹H NMR spectra of standard ¹⁵NH₄⁺, ¹⁴NH₄⁺, and the sample by using ¹⁴N₂ and ¹⁵N₂ as the feeding gas yields, respectively. (d) FE and NH₃ production rate during the recycling test under the potential of -0.4 V vs. RHE.

To conclude on the influence of oxygen substitution by carbon in the anion lattice of TiO_2 , NRR performance of M-800 and M-900 is also tested. At the potential of -0.4 V vs. RHE, FE and NH_3 production rate of M-800 and M-900 lag far behind M-1000 (Figure S23) but with a stronger HER (Figure S16b). As for M-1100, both FE and NH_3 production rate go down again. Further considering the different content of doped carbon in M-Ts (Table S1), we suspect that the formed (O-)Ti-C bonds in $\text{C-Ti}_x\text{O}_y$ are the most favourable active sites for N_2 fixation. Based on previously published results, OVs in $\text{C-Ti}_x\text{O}_y$ could also act active sites.³² However, comparison of the NRR performance of M-Ts reveals that (O-)Ti-C bonds may play a more important role in NRR than non-substituted OVs and Ti-C bonds as present in crystalline titanium carbide. The amount of OVs and Ti-C bonds in M-1100 is much higher as compared to M-1000 but this material has inferior NRR performance. Besides, NRR performance was tested by using commercial TiO_2 catalysts without any carbon doping, which show bad NRR performance (Figure S23). The same result was also observed in commercial TiC catalysts. Although there are enough Ti-C bonds existing, they are not as active as (O-)Ti-C bonds in C-doped Ti_xO_y , where C atoms can replace OVs. In addition, the electrochemical active surface area (ECSA) of M-1000 in 0.1 M N_2 -saturated LiClO_4 is larger than those of M-800, M-900 and M-1100 clearly confirmed that the more active sites of M-1000 (Figure S24 and S25). Besides, a N_2 adsorption test at different temperatures (Figure S26 a and b) was conducted to investigate the N_2 affinity of as-obtained M-Ts by calculating the heat of adsorption (Q_{st}) of N_2 (Figure S26c), which shows that M-1000 has the strongest N_2 affinity and thus better N_2 activation ability. In contrast to the M-Ts materials, the N species in M-Ts- N_2 are electrochemically unstable, as NH_3 can also be detected without N_2 as feeding gas after the chronoamperometry test (Figure S27). In order to further demonstrate that (O-)Ti-C bonds present in Ti_xO_y are the active sites in M-1000, commercial TiO_2 is mixed with the MOF linker terephthalic acid (H_2BDC) and treated under the same conditions as M-1000 (sample denoted as C-treated TiO_2). In this way, a comparable structure to M-1100 consisting of carbon-doped Rutile and TiC was fabricated with the small nanoparticles embedded into the carbon (Figure S28). The NRR performance of C-treated TiO_2 is dramatically improved to the decent FE of 8% after carbon doping (Figure S29). This further indicates that C doping and (O-)Ti-C bond formation in TiO_2 are crucial for the N_2 activation. The apparently higher crystalline TiC content in C-treated TiO_2 and its lower SSA are likely responsible for the lower FE in comparison to M-1000. As a comparison, TiO_2 was also treated under the same conditions in absence of H_2BDC . The resulting material exhibited a much worse NRR performance (Figure S29). Therefore, the success of C-treated TiO_2 in NRR also demonstrates that this anion substitution is applicable and universal for constructing efficient NRR electrocatalysts.

To gain deep insights into the origin of the enhanced NRR performance of M-1000 catalyst and to highlight the role of carbon doping in NRR, density functional theory (DFT) calculations were carried out to investigate the mechanism of N_2 fixation on the C-doped TiO_2 (110) surface ($\text{C-Ti}_x\text{O}_y$) compared with non-doped OVs enriched TiO_2 (OVs- TiO_2). The computational methods and rationalized surface models (Figure S30 and Figure S31) as well as the optimized surface

intermediates and their energies are given, respectively (Figure S32 and Figure S33). According to the typical NRR distal pathway and the corresponding free energy diagram through the distal mechanisms of NRR on $\text{C-Ti}_x\text{O}_y$ surface (Figure 4), N_2 is firstly adsorbed on the carbon site with an energy gain of -0.06 eV. It is also found that charge density difference between N_2 and C on the defect in $\text{C-Ti}_x\text{O}_y$ is larger than that between N_2 and OVs in OVs- TiO_2 (Figure S34). This clearly indicates that the doped carbon sites can more strongly activate N_2 and serve active sites for NRR. The key step of the first hydrogenation of C^*N_2 to C^*NNH is endergonic by 0.64 eV; and the N-N distance is elongated from 1.17 Å to 1.25 Å during this process. The subsequent formation of C^*NNH_2 from C^*NNH hydrogenation is exergonic by 0.49 eV. Similarly, this step is also accompanied by the elongation of the N-N distance from 1.25 Å to 1.36 Å. The next step, which involves the N-N dissociation as well as forms surface N^* and the first NH_3 gas molecule, is exergonic by 1.47 eV. The subsequent stepwise hydrogenation of surface C^*N to surface C^*NH and C^*NH_2 as well the formation of the second NH_3 gas molecule is endergonic by 0.41 , 0.01 , and 0.26 eV, respectively.

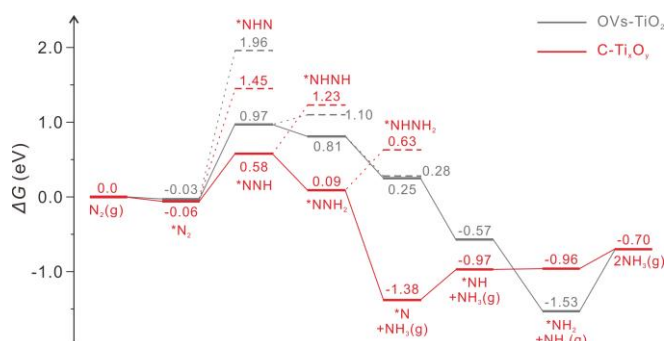


Figure 4. Free energy surface (G , eV, 298.15 K) for NRR on $\text{C-Ti}_x\text{O}_y$ (110) (red) and OVs- TiO_2 (110) (gray) (solid line for the more favored route and dotted line for the less favored route on the corresponding surface).

On the non-doped OVs- TiO_2 , similar reaction path is found (Figure 4 and Figure S33). After the adsorption of N_2 on the surface (-0.03 eV), the formation of surface $^*\text{NNH}$ is endergonic by 1.00 eV, while the formation of surface $^*\text{NNH}_2$ as well as $^*\text{N}$ and NH_3 gas molecule is exergonic by 0.16 and 0.56 eV, respectively. The subsequent hydrogenation of surface $^*\text{N}$ to surface $^*\text{NH}$ and $^*\text{NH}_2$ is exergonic by 0.82 and 0.96 eV, respectively, while the formation of gas NH_3 molecule is endergonic by 0.83 eV.

It is also worth to note that the $^*\text{NHN}$, $^*\text{NHNH}$ and $^*\text{NHNH}_2$ surface species have higher energy and are thus less stable than the corresponding $^*\text{NNH}$, $^*\text{NNH}_2$ and $^*\text{N}+\text{NH}_3(\text{g})$ intermediates (Figure S32), indicating that the formation of diazene ($\text{HN}=\text{NH}$) and hydrazine ($\text{H}_2\text{N}-\text{NH}_2$) is not favored thermodynamically which also fully agree with the experimental observations.

Further comparison of the above reaction free energies on $\text{C-Ti}_x\text{O}_y$ and OVs- TiO_2 demonstrates that the first step of N-H^{*} formation is the potential-determining step in the electrochemical NRR; and most importantly $\text{C-Ti}_x\text{O}_y$ is more active than OVs- TiO_2 (0.64 vs. 1.00 eV). Therefore, this advantageous low energy barrier on $\text{C-Ti}_x\text{O}_y$ can significantly enhance the electrocatalytic

activity for the NRR, which is in agreement with the experimental results.

In conclusion, we have presented a novel mode for activation of N₂ by carbon-doped sites in the anion lattice of Rutile. An efficient NRR catalyst of C-Ti_xO_y/C nanocomposite has been developed via simple pyrolysis of MIL-125(Ti). The density of covalent Ti-C bonds originating from carbon atoms and OVs (which can both be active sites for NRR) can be regulated by the synthesis temperature. By comparing the NRR performance of M-Ts and by carrying out DFT calculations, we found that the existence of (O-)Ti-C bonds in C-doped Ti_xO_y can largely improve the ability to activate and reduce N₂ as compared to unoccupied OVs in TiO₂. Given by the development of nanotechnology, the strategy of rationally doping heteroatoms into the anion lattice of transition metal oxides to create active centers may open many new opportunities beyond the use of noble metal-based catalysts for other reactions that require the activation of small molecules as well.

Acknowledgements

We thank Dr. Heike Runge for providing the SEM measurements. We also thank Dr. Antje Voelkel for the elemental analyses and TGA measurements. Funded by the Deutsche Forschungsgemeinschaft (DFG, German Research Foundation) under Germany's Excellence Strategy – EXC 2008/1 (UniSysCat) – 390540038.

Keywords: MOF-derived catalysts • anion substitution • non-noble metal catalysts • N₂ fixation • ammonia synthesis

- [1] a) C. Zamfirescu, I. Dincer, *J. Power Sources* **2008**, *185*, 459-465; b) J. W. Erisman, M. A. Sutton, J. Galloway, Z. Klimont, W. Winiwarter, *Nat. Geosci.* **2008**, *1*, 636-639; c) K. A. Brown, D. F. Harris, M. B. Wilker, A. Rasmussen, N. Khadka, H. Hamby, S. Keable, G. Dukovic, J. W. Peters, L. C. Seefeldt, P. W. King, *Science* **2016**, *352*, 448-450.
- [2] a) D. Bao, Q. Zhang, F. L. Meng, H. X. Zhong, M. M. Shi, Y. Zhang, J. M. Yan, Q. Jiang, X. B. Zhang, *Adv. Mater.* **2017**, *29*, 1604799; b) S. Chen, S. Perathoner, C. Ampelli, C. Mebrahtu, D. Su, G. Centi, *Angew. Chem. Int. Ed.* **2017**, *56*, 2699-2703; c) C. X. Guo, J. R. Ran, A. Vasileff, S. Z. Qiao, *Energy Environ. Sci.* **2018**, *11*, 45-56.
- [3] A. E. Shilov, *Russ. Chem. Bull.* **2003**, *52*, 2555-2562.
- [4] a) A. R. Singh, B. A. Rohr, J. A. Schwalbe, M. Cargnello, K. Chan, T. F. Jaramillo, I. Chorkendorff, J. K. Nørskov, *ACS Catal.* **2016**, *7*, 706-709; b) J. M. McEnaney, A. R. Singh, J. A. Schwalbe, J. Kibsgaard, J. C. Lin, M. Cargnello, T. F. Jaramillo, J. K. Nørskov, *Energy Environ. Sci.* **2017**, *10*, 1621-1630; c) G. F. Chen, X. Cao, S. Wu, X. Zeng, L. X. Ding, M. Zhu, H. Wang, *J. Am. Chem. Soc.* **2017**, *139*, 9771-9774.
- [5] a) A. J. Martín, T. Shinagawa, J. Pérez-Ramírez, *Chem* **2018**, *5*, 1-21; b) G.-F. Chen, S. Ren, L. Zhang, H. Cheng, Y. Luo, K. Zhu, L.-X. Ding, H. Wang, *Small Methods* **2019**, *3*, 1800337.
- [6] M. M. Shi, D. Bao, B. R. Wulan, Y. H. Li, Y. F. Zhang, J. M. Yan, Q. Jiang, *Adv. Mater.* **2017**, *29*, 1606550.
- [7] a) Z. Wang, F. Gong, L. Zhang, R. Wang, L. Ji, Q. Liu, Y. Luo, H. Guo, Y. Li, P. Gao, X. Shi, B. Li, B. Tang, X. Sun, *Adv. Sci.* **2019**, *6*, 1801182; b) C. Lv, C. Yan, G. Chen, Y. Ding, J. Sun, Y. Zhou, G. Yu, *Angew. Chem. Int. Ed.* **2018**, *57*, 6073-6076.
- [8] a) R. Zhang, Y. Zhang, X. Ren, G. W. Cuo, A. M. Asiri, B. Z. Zheng, X. P. Sun, *ACS Sustain. Chem. Eng.* **2018**, *6*, 9545-9549; b) X. Ren, G. Cui, L. Chen, F. Xie, Q. Wei, Z. Tian, X. Sun, *Chem. Commun.* **2018**, *54*, 8474-8477.
- [9] a) H. Cheng, L. X. Ding, G. F. Chen, L. Zhang, J. Xue, H. Wang, *Adv. Mater.* **2018**, *30*, 1803694; b) Y. Luo, G.-F. Chen, L. Ding, X. Chen, L.-X. Ding, H. Wang, *Joule* **2018**, *3*, 1-11.
- [10] E. Y. Jeong, C. Y. Yoo, C. H. Jung, J. H. Park, Y. C. Park, J. N. Kim, S. G. Oh, Y. Woo, H. C. Yoon, *ACS Sustain. Chem. Eng.* **2017**, *5*, 9662-9666.
- [11] a) X. M. Yu, P. Han, Z. X. Wei, L. S. Huang, Z. X. Gu, S. J. Peng, J. M. Ma, G. F. Zheng, *Joule* **2018**, *2*, 1610-1622; b) Y. Song, D. Johnson, R. Peng, D. K. Hensley, P. V. Bonnesen, L. Liang, J. Huang, F. Yang, F. Zhang, R. Qiao, A. P. Baddorf, T. J. Tschaplinski, N. L. Engle, M. C. Hatzell, Z. Wu, D. A. Cullen, H. M. Meyer, 3rd, B. G. Sumpter, A. J. Rondinone, *Sci. Adv.* **2018**, *4*, e1700336.
- [12] Q. Qin, T. Heil, M. Antonietti, M. Oschatz, *Small Methods* **2018**, *2*, 1800202.
- [13] a) G.-F. Chen, X. Cao, S. Wu, X. Zeng, L.-X. Ding, M. Zhu, H. Wang, *J. Am. Chem. Soc.* **2017**, *139*, 9771-9774; b) X. Li, T. Li, Y. Ma, Q. Wei, W. Qiu, H. Guo, X. Shi, P. Zhang, A. M. Asiri, L. Chen, B. Tang, X. Sun, *Adv. Energy Mater.* **2018**, *8*, 1801357; c) Y. Fang, Z. Liu, J. Han, Z. Jin, Y. Han, F. Wang, Y. Niu, Y. Wu, Y. Xu, *Adv. Energy Mater.* **2019**, *9*, 1803406.
- [14] a) X. Zhang, Q. Liu, X. Shi, A. M. Asiri, Y. Luo, X. Sun, T. Li, J. Mater. Chem. A **2018**, *6*, 17303-17306; b) L. Yang, T. Wu, R. Zhang, H. Zhou, L. Xia, X. Shi, H. Zheng, Y. Zhang, X. Sun, *Nanoscale* **2019**, *11*, 1555-1562; c) R. Zhang, X. Ren, X. Shi, F. Xie, B. Zheng, X. Guo, X. Sun, *ACS Appl. Mater. Inter.* **2018**, *10*, 28251-28255.
- [15] Y. Wang, K. Jia, Q. Pan, Y. Xu, Q. Liu, G. Cui, X. Guo, X. Sun, *ACS Sustain. Chem. Eng.* **2019**, *7*, 117-122.
- [16] a) K. Shen, X. D. Chen, J. Y. Chen, Y. W. Li, *ACS Catal.* **2016**, *6*, 5887-5903; b) H. L. Jiang, B. Liu, Y. Q. Lan, K. Kuratani, T. Akita, H. Shioyama, F. Zong, Q. Xu, *J. Am. Chem. Soc.* **2011**, *133*, 11854-11857.
- [17] S. N. Kim, J. Kim, H. Y. Kim, H. Y. Cho, W. S. Ahn, *Catal. Today* **2013**, *204*, 85-93.
- [18] W. K. Wang, J. J. Chen, X. Zhang, Y. X. Huang, W. W. Li, H. Q. Yu, *Sci. Rep.* **2016**, *6*, 20491.
- [19] C. H. Huang, D. Gu, D. Y. Zhao, R. A. Doong, *Chem. Mater.* **2010**, *22*, 1760-1767.
- [20] B. H. Lohse, A. Calka, D. Wexler, *J. Alloys Compd.* **2007**, *434*, 405-409.
- [21] S. Mohapatra, D. K. Mishra, S. K. Singh, *Powder Technol.* **2013**, *237*, 41-45.
- [22] D. Portehault, V. Maneeratana, C. Candolfi, N. Oeschler, I. Veremchuk, Y. Grin, C. Sanchez, M. Antonietti, *ACS Nano* **2011**, *5*, 9052-9061.
- [23] J. Schnadt, J. N. O'Shea, L. Patthey, J. Schiessling, J. Krempasky, M. Shi, N. Martensson, P. A. Bruhwiler, *Surf. Sci.* **2003**, *544*, 74-86.
- [24] K. Krishnamoorthy, P. Pazhamalai, S. Sahoo, S. J. Kim, *J. Mater. Chem. A* **2017**, *5*, 5726-5736.
- [25] a) F. Dong, S. Guo, H. Wang, X. F. Li, Z. B. Wu, *J. Phys. Chem. C* **2011**, *115*, 13285-13292; b) Y. Huang, W. Ho, S. Lee, L. Zhang, G. Li, J. C. Yu, *Langmuir* **2008**, *24*, 3510-3516.
- [26] E. A. Reyes-Garcia, Y. Sun, K. R. Reyes-Gil, D. Rafferty, *Solid State Nucl. Magn. Reson.* **2009**, *35*, 74-81.
- [27] T. Oshikiri, K. Ueno, H. Misawa, *Angew. Chem. Int. Ed.* **2016**, *55*, 3942-3946.
- [28] S. Z. Andersen, V. Čolić, S. Yang, J. A. Schwalbe, A. C. Nielander, J. M. McEnaney, K. Enemark-Rasmussen, J. G. Baker, A. R. Singh, B. A. Rohr, M. J. Statt, S. J. Blair, S. Mezzavilla, J. Kibsgaard, P. C. K. Vesborg, M. Cargnello, S. F. Bent, T. F. Jaramillo, I. E. L. Stephens, J. K. Nørskov, I. Chorkendorff, *Nature* **2019**, DOI:10.1038/s41586-019-1260-x.